Multi-Material Topology Optimization of an eVTOL PAV Wing Considering Additive Manufacturing

T. Sirola[a], O. Pintar[a], and I. Y. Kim[a]

[a]Department of Mechanical and Materials Engineering, Queen's University

E-mail: kimiy@queensu.ca

Abstract

As global populations continue to rise, the limitations of conventional ground transport have become increasingly evident, necessitating the development of alternative modes of transportation in urban centres. This has led to significant research in Urban Air Mobility (UAM), where engineers are working to develop electric vertical take-off and landing personal air vehicles (eVTOL PAVs) as an alternative mode of short to mid-range transportation. The loads experienced by these aircrafts are inherently different than those of conventional aircraft, presenting the opportunity for the development of novel structural designs. This can be achieved using topology optimization (TO), a computational design tool capable of determining the optimal material layout given a design envelope and constraints. The goal of this work is to leverage multi-material topology optimization (MMTO) to generate superior wing and wing-fuselage joining structures for eVTOL PAV applications which may be suitable for additive manufacturing. The optimization considers aerodynamic pressure loading from multiple maneuver and gust conditions, as well as VTOL and cruise thrust loading unique to PAV applications. Multiple material combinations are tested, and direct comparisons between optimal single and multi-material designs are conducted to demonstrate the benefits of multi-material optimization in PAV design. The work presented here includes the results of preliminary MMTO studies for PAV internal wing structures.

Keywords –

Multi-material topology optimization, Personal air vehicles, Urban air mobility

1 Introduction

Single material topology optimization (SMTO) has been used extensively in the design of lightweight aerospace structures, as outlined by the review in [1]. However, applications of more advanced optimization techniques, such as multi-material topology optimization (MMTO), remain relatively unexplored within the aerospace industry due to various numerical and practical challenges. This research aims to demonstrate the effectiveness of MMTO for complex aerospace applications.

MMTO acts to further extend the design freedom of the solver by allowing for optimal selection of both material type and placement, yielding designs with enhanced structural performance. Furthermore, advancements in additive manufacturing (AM) techniques have made it possible to feasibly manufacture the complex geometries often generated through topology optimization, such that the final design may remain closer to the optimal material layout. The coupling of MMTO with AM presents the opportunity for a powerful conceptual design tool for aerospace applications.

The objective of this research is to develop novel lightweight PAV wing and wing-fuselage joining structures by leveraging multi-material topology optimization. The work presented in this conference will include the first stage of the multi-material topology optimization activity, which focuses on the development of conceptual level internal wing structures.

2 Methodology

2.1 Concept Generation

As a starting point for this work, a complete PAV design concept was developed in OpenVSP. To generate the initial concept, an aircraft sizing and resizing process was completed based on the methods presented in [2] using a maximum takeoff weight (MTOW) target of 1500kg, a range of 110km, and a cruise speed of 200km/h.

Subsequent static stability analysis was conducted using VSPAERO, and adjustments were made as required to achieve acceptable stability response in pitch and yaw (roll is not considered at this stage). A schematic of the initial design concept is shown in Figure 1 below. The propellor-bearing mid wing was

selected as an initial target structure due to the unconventional loads resultant from the wing mounted VTOL and forward propulsors.

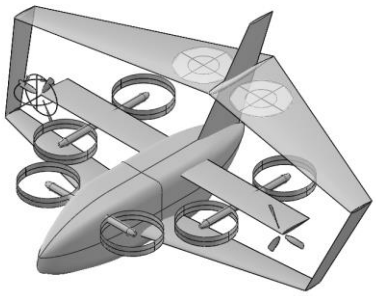

Figure 1: An image of the conceptual PAV design.

2.2 Load Development

The loads considered for the analysis and optimization can be broadly categorized into aerodynamic loads and propulsion loads. In order to establish appropriate aerodynamic loading states, a V-n diagram was developed based on the requirements for normal aircraft outlined in Part 23 of the Federal Aviation Regulations [3] (FARs) in conjunction with the procedure presented in [4]. The V-n diagram for the PAV concept is shown in Figure 2.

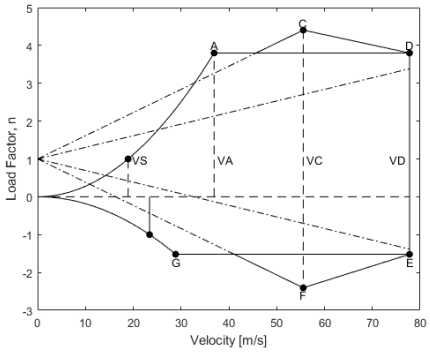

Figure 2: The V-n diagram for the PAV concept.

The most extreme loads occur at the limits of the flight envelope and must be considered during optimization. Therefore, four load states from the V-n diagram were selected for use in optimization, as shown in Table 1. An additional safety factor of 1.5 was applied based on the FARs requirement.

Table 1: Key flight states for the PAV based on the V-n diagram.

Condition	Velocity [m/s]	n [g]	n x SF [g]
+ Maneuver (A)	36.91	3.80	5.70
- Maneuver (G)	28.87	-1.52	-2.28
+ Gust (C)	55.56	4.40	6.60
- Gust (F)	55.56	-2.40	-3.60

Since the current modelling approach only considers static loading, an equivalent flight state (angle of attack) for each load factor can be determined based on the lift force generated by the airfoil. First, the amount of lift required to cause the desired load factor is calculated using Equation 1,

$$L_{req} = nMTOW \qquad (1)$$

where L_{req} is the desired lift force, n is desired load factor, and $MTOW$ is the maximum takeoff weight. Then, aerodynamic analysis is performed in VSPAERO for a range of angles of attack at the velocity corresponding to the desired load factor. From this analysis, the coefficient of lift (C_L) as a function of angle attack is obtained. This can then be converted to a plot of the lift force as a function of angle of attack using Equation 2,

$$L = \frac{1}{2} C_L \rho V^2 S \qquad (2)$$

where L is the lift force, C_L is the coefficient of lift, ρ is the freestream density, V is the aircraft velocity (from the V-n diagram), and S is the projected wing area. Finally, using the plot of lift force vs. angle of attack, and the required lift as calculated from Equation 1, the equivalent angle of attack state for each desired load factor can be determined as shown in Table 2.

Table 2: The critical flight states and the corresponding equivalent angle of attack.

Condition	Velocity [m/s]	n x SF [g]	AoA [°]
+ Maneuver (A)	36.91	5.70	16.53
- Maneuver (G)	28.87	-2.28	-10.10
+ Gust (C)	55.56	6.60	8.66
- Gust (F)	55.56	-3.60	-4.02

The aerodynamic loads on the wing can be captured by measuring the pressure distribution over its surface. The pressure distribution over a wing is typically represented by the non-dimensionalized coefficient C_p as defined by Equation 3,

$$C_p = \frac{p - p_\infty}{\frac{1}{2}\rho_\infty V_\infty^2} \qquad (3)$$

where p is the pressure at any point on the airfoil surface, p_∞ is the freestream static pressure, V_∞ is the freestream fluid velocity (taken to be equal to the aircraft speed), and ρ_∞ is the freestream fluid velocity. To obtain the C_p distribution over the airfoil at each of the four flight conditions, aerodynamic analysis was performed in VSPAERO. Figure 3 shows the resultant C_p distribution for each of the critical flight states.

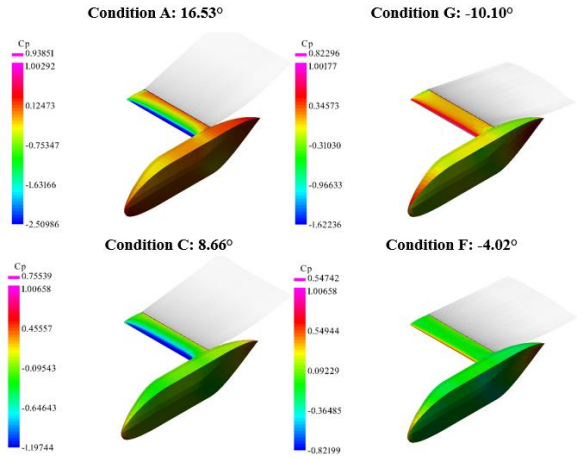

Figure 3: Contours of the C_p distribution for each of the critical flight states.

Here it is observed that for positive angles of attack (condition A and C), a negative C_p, indicating a pressure below the freestream pressure, is observed on the top surface near the leading edge. This is expected as the pressure differential between the top and bottom surfaces of the airfoil generates a net positive lift force at a positive angle of attack. Conversely, a positive C_p is observed on the top surface at negative angles of attack (condition G and F) which is expected as this generates a net downward force on the wing.

The pressure distribution over the wing varies along the span and must be captured to ensure adequate fidelity of the aerodynamic loading conditions used for optimization. As such, the C_p slicer tool in VSPAERO was used to extract C_p data at equidistant discrete chordwise sections of the wing as shown in Figure 4. For each chord section plane along the wing (shown in grey), a complete C_p distribution over the airfoil is obtained, which can be used to map the change in pressure distribution along the wingspan. Examples of the pressure distribution at the root and tip of the wing are shown Figure 4.

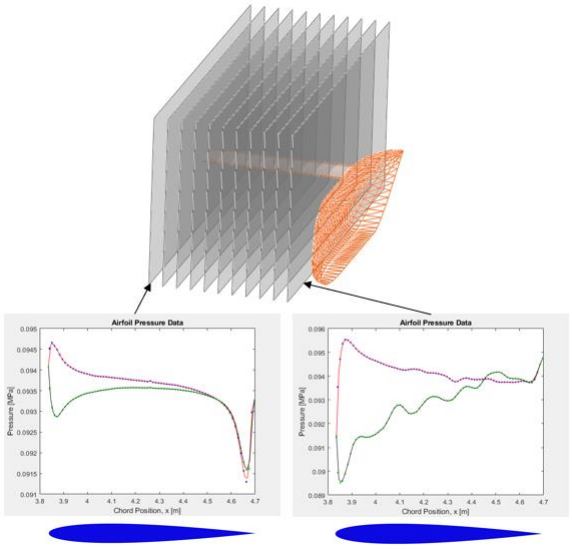

Figure 4: An example of the C_p slicer tool in VSPAERO and resulting C_p distributions at the root and tip of the wing.

The raw C_p data for each section plane was imported into MATLAB for postprocessing, where it was converted to physical pressure and fit using built-in interpolation functions (see Figure 4). The fit pressure data was used to apply surface pressure loads to specific elements in the finite element model at locations corresponding to the section planes in Figure 4. More details of pressure load application within the finite element model are provided in Section 2.3.

The remaining loads considered in the optimization are due the forward cruise and VTOL propulsors shown in Figure 1. The largest VTOL loading experienced by the wing structure occurs during take-off and climb conditions where the thrust to weight ratio is defined by Equation 4 [2],

$$(T/W)^{VTOL}_{\text{climb}} = 1.2\left(1 + \frac{1}{W/S_w}\rho(R/C)^2(S_{tot}/S_w)\right) \qquad (4)$$

where T is the total thrust, W is the aircraft weight, S_w is the project wing area, S_{tot} is the total projected area of aircraft, ρ is the freestream air density, and R/C is the rate of vertical climb. The thrust load for each VTOL propellor can then be calculated from Equation 5,

$$T^{VTOL}_{prop} = \frac{1.2}{n_{prop}} W\left(1 + \frac{1}{W/S_w}\rho(R/C)^2(S_{tot}/S_w)\right) \qquad (5)$$

where T^{VTOL}_{prop} is the thrust load from each VTOL propellor, and n_{prop} is the number of VTOL propellors (8 in this design).

Two different VTOL loading conditions are considered for optimization as shown in Figure 5. The first, referred to as regular operation, has VTOL thrust loads applied to each of the wing mounted VTOL propellors. The second configuration assumes catastrophic failure of one of the wing mounted propellors. In this case, a force with a magnitude of twice the VTOL thrust force is applied to only one of the rotor locations, assuming the functional propellor must compensate for the failure to maintain balanced lateral thrust.

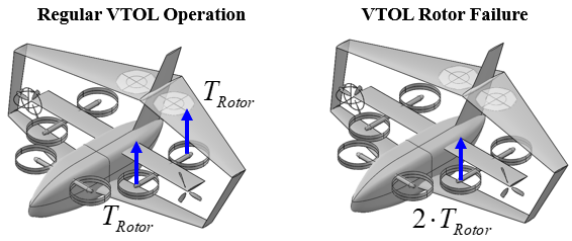

Figure 5: The two different VTOL operating conditions considered for load development.

The largest load caused by the wingtip mounted forward propulsor occurs during a forward climb condition, where the thrust to weight ratio is defined by Equation 6 [2],

$$(T/W)^{FW}_{climb} = \frac{R/C}{V_{RoC}} + \frac{q}{W/S_W} C_{D_0} + \frac{k}{q}(W/S_W) \qquad (6)$$

where C_{D_0} is the minimum drag coefficient, V_{RoC} is the forward rate of climb velocity, q is the dynamic pressure and, k is a lift-induced drag constant. The thrust load for one propulsor is given by Equation 7,

$$T^{FW}_{prop} = \frac{W}{n_{prop}} \left(\frac{R/C}{V_{RoC}} + \frac{q}{W/S_W} C_{D_0} + \frac{k}{q}(W/S_W) \right) \qquad (7)$$

where T^{FW}_{prop} is the thrust load from each forward propellor.

2.3 Finite Element Model

In order to perform analysis and optimization, a finite element model of the wing was generated using Altair Hypermesh. The model the wing consists of 194,123 elements with an average element size of 10 mm. As shown in Figure 6, the interior of the wing (yellow), which is comprised of 137,921 3D elements, is designated as the design space for optimization. The design space is surrounded by a non-designable skin of 2D shell elements (blue) upon which the aerodynamic pressure loads were applied.

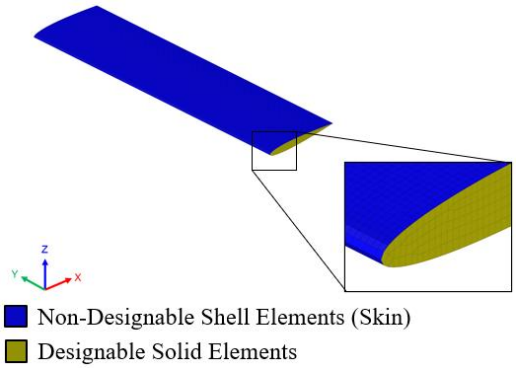

Figure 6: An image of the wing finite element model.

Aerodynamic pressure loads were applied according to the procedure shown in Figure 7. The pressure curves generated in MATLAB were used to apply appropriate pressure loads along rows of skin elements corresponding to the location of the section planes from VSPAERO (see Figure 7a). A linear interpolation between each discrete row of pressure loads was then completed using built-in functionality in Optistruct to generate a complete pressure distribution over the wing surface (see Figure 7b).

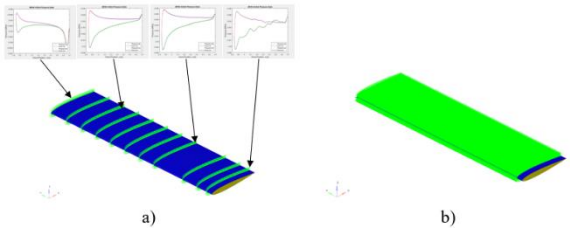

Figure 7: A schematic of the pressure application process showing a) the application of pressures at discrete span locations, and b) the complete pressure distribution after linear interpolation.

This process was repeated for each of the four flight states from Table 2, to generate four individual aerodynamic load cases in the model as shown in Figure 8.

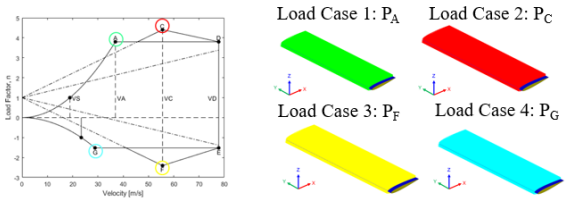

Figure 8: The four pressure load cases for each flight state identified on the V-n diagram.

The VTOL rotor booms were modelled as rigid RBE3 elements to reduce the size of the model, and the

associated computational cost of optimization. VTOL propellor loads were then applied as point forces directly to the ends of the rigid boom elements. The forward cruise thrust load was applied to rigid elements at the wing tip which transfer the load to nodes along the edge of the non-designable skin. Propellor mass loads were also applied at the VTOL booms and wing tip based on mass results from the component sizing process. Figure 9 and Table 3 show the magnitude and location of each type of propellor load applied to the model.

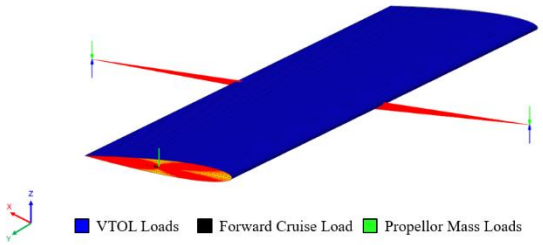

Figure 9: A schematic of the point loads applied for each of the propeller loads.

Table 3: The magnitude and location of each propellor load applied to the finite element model.

Load Case	Force [N]	Location
Forward Cruise	-1798.7 (X)	Wing Tip
Normal VTOL	3391.2 (Z)	Booms
VTOL Fail 1	6782.4 (Z)	Fore Boom
VTOL Fail 2	6782.4 (Z)	Aft Boom
Propellor Mass	-163.5 (Z)	Booms
	-209.1 (Z)	Wing Tip

2.4 Multi-Material Topology Optimization

The most commonly used method in structural topology optimization is a density-based approach in which the design variables represent the pseudo-densities of each element in the design space. By varying the element pseudo-density, the optimizer is able to determine material existence between solid (1) and void (0). The pseudo-density can then be related to element properties, like stiffness, through a material interpolation scheme such as the solid isotropic material with penalization (SIMP) method. For TO with a single material, the SIMP interpolation schemes for mass and stiffness are given by Equations 8 and 9:

$$W\left(\underset{\sim}{\rho}\right) = \underset{\sim}{\rho}^{q} W_0 \tag{8}$$

where W is the mass of the interpolated element, ρ is the design variable vector, q is a penalty factor to penalize intermediate densities (normally q=1), and W_0 is the mass of the solid element.

$$E\left(\underset{\sim}{\rho}\right) = \underset{\sim}{\rho}^{p} E_0 \tag{9}$$

where E is the stiffness of the interpolated element, ρ is the design variable vector, p is a penalty factor to penalize intermediate densities (normally p=3), and E_0 is the stiffness of the solid element.

In MMTO, the solver determines material existence and material selection simultaneously, necessitating the addition of material selection design variables. For MMTO with M material phases, ρ^1 represents the material existence design variable, and $\rho^2, \ldots, \rho^{M-1}$ represent material selection design variables. Therefore, the SIMP method requires modification for use with multiple materials. For MMTO, the SIMP formulation can be extended to M material phases (M-1 materials and one void) using Equations 10 and 12 [5]:

$$W^{(1,\ldots,M)}\left(\underset{\sim}{\rho}^1, \ldots, \underset{\sim}{\rho}^{M-1}\right) = \sum_{i=1}^{M} \underset{\sim}{\alpha}_i W^{(M-i+1)} \tag{10}$$

where

$$\underset{\sim}{\alpha}_i = \left[1 - \left(\underset{\sim}{\rho}^i - \underset{\sim}{\rho}^i \delta_{iM}\right)^q\right] \prod_{i}^{i-1} \left(\underset{\sim}{\rho}^t\right)^q$$
$$\delta_{iM} = \begin{cases} 1, i = M \\ 0, i \neq M \end{cases} \tag{11}$$

where ρ^j is the jth nominal density, $W^{(j)}$ is the original mass of the element with the jth material, and $W^{(1,\ldots,M)}$ is the interpolated element mass.

$$E^{(1,\ldots,M)}\left(\underset{\sim}{\rho}^1, \ldots, \underset{\sim}{\rho}^{M-1}\right) = \sum_{i=1}^{M} \underset{\sim}{\beta}_i E^{(M-i+1)} \tag{12}$$

where

$$\underset{\sim}{\beta}_i = \left[1 - \left(\underset{\sim}{\rho}^i - \underset{\sim}{\rho}^i \delta_{iM}\right)^p\right] \prod_{i}^{i-1} \left(\underset{\sim}{\rho}^t\right)^p$$
$$\delta_{iM} = \begin{cases} 1, i = M \\ 0, i \neq M \end{cases} \tag{13}$$

where $E^{(j)}$ is the original stiffness of the element with the jth material, and $E^{(1,\ldots,M)}$ is the interpolated element stiffness.

This work will consider optimization with up to 5 material phases (4 materials and void) in MMTO. The materials and their relevant properties are listed in Table 4. Note that only isotropic materials (with the same Poisson's ratio) are compatible with the SIMP scheme outlined above, and integration of anisotropic materials is left for future work.

Table 4: Materials used for MMTO.

Material	E [GPa]	ν	ρ [kg/m³]
Steel	210	0.33	7850
Titanium	110	0.33	4500
Aluminum	70	0.33	2700
CF SMC	33	0.33	1460

The optimization problem applied in this research considers a mass minimization objective with the following problem statement:

$$\underset{\underset{\sim}{\rho}^1,\underset{\sim}{\rho}^2,\ldots,\underset{\sim}{\rho}^{m-1},\underset{\sim}{\rho}^m}{Minimize} \quad W\left(\underset{\sim}{\rho}^j\right)$$
$$Subject\ to \quad |u_i| \le \bar{u}_i,\ i = 1,\ldots,9$$
$$\underset{\sim}{\underset{\sim}{K}}\,\underset{\sim}{u} = \underset{\sim}{f}$$
$$\forall\, element\, e, \rho_e^j \in (0,1],\ j = 1,\ldots,m$$

where W is the total mass of the designable elements, u_i is the nodal displacement at a prescribed node, $\bar{u}_i$ is the magnitude of the defined displacement constraint at a prescribed node, and $\underset{\sim}{\underset{\sim}{K}}\,\underset{\sim}{u} = \underset{\sim}{f}$ is the governing equation for linear elasticity. The displacement constraints applied in this model were generated by running a compliance minimization with a 30% mass fraction and extracting nodal displacements at nodes of interest (wing tip and VTOL booms) for each load case. For this work, a custom FORTRAN solver which directly interfaces with Optistruct for finite element analysis, and then solves the optimization problem using the gradient-based method of moving asymptotes (MMA) was used for MMTO implementation.

3 Results

3.1 Single Material Topology Optimization

As a starting point for the optimization activity, SMTO using aluminum was performed. The mass of the converged SMTO result was found to be 148.48 kg. An ISO plot of the aluminum SMTO result is shown in Figure 10. The results of the aluminum SMTO will be used as a baseline to evaluate the performance of subsequent MMTO studies.

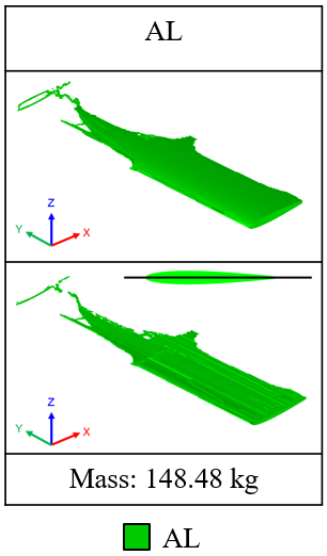

Figure 10: An ISO plot of the SMTO results, including a section view showing the internal structure of the wing.

From Figure 10, it can be seen that the optimization places a significant amount of material between the root and the VTOL booms. There also appear to be spar-like structures forming within this region, and a rib structure spanning the cross section at the location of the rigid boom elements. Towards the tip of the wing, there is a curved I-beam-like structure which transfers the load to a partial rib structure at the wing tip.

3.2 Multi-Material Topology Optimization

For this initial implementation, four different material combinations were tested within the MMTO framework: Aluminum – CF SMC, Aluminum – Steel, Aluminum – Titanium, and Aluminum – Steel – Titanium – CF SMC. The MMTO results for each of these material combinations are shown in Figure 11.

The MMTO results exhibit similar structures to that of the SMTO structure shown in Figure 10. For cases which include materials that are stiffer than aluminum (steel / titanium) the solver favours placing large sections of the stiffer material at the extremities of the design space near the root. This maximizes the resistance to the bending moments caused by the aerodynamic and VTOL loads without utilizing a significant volume of internal support structures.

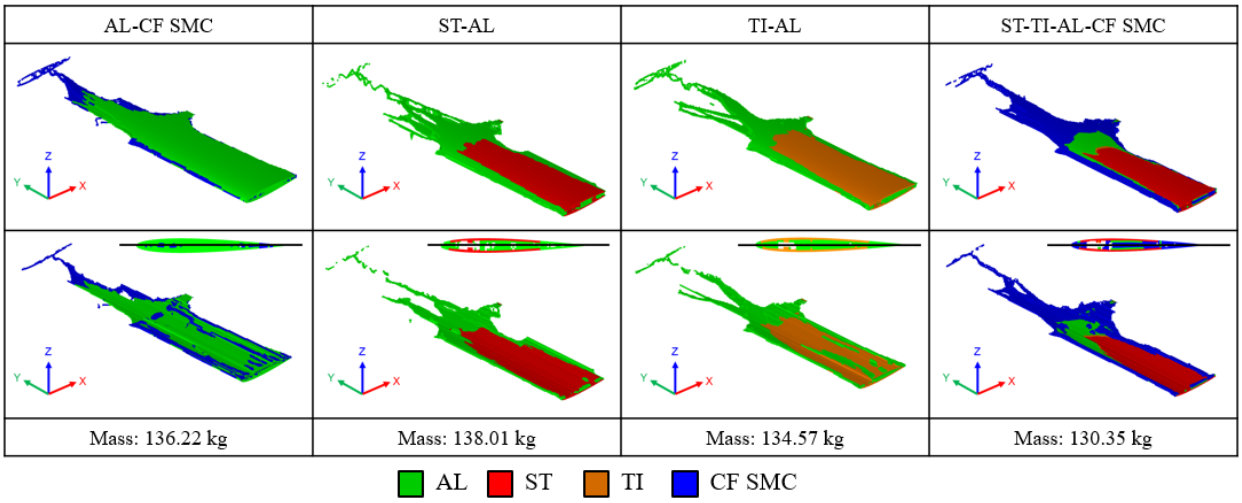

Figure 11: Plots of the results for each of the material combinations used in MMTO. Bottom images include section planes for viewing of internal structures.

When a less stiff material is used, such as CF SMC, the solver favours placing a significant amount of smaller support structures on the interior of the wing to reinforce the top and bottom aluminum structures. This is a feasible solution in this case due to the low density of the composite material.

3.3 Design Comparison

The mass results for each of the TO designs presented in Figure 10 and Figure 11 are summarized in Table 5.

Table 5: A comparison of the optimized mass for each TO result.

Design	Mass [kg]
AL (SMTO)	148.48
AL – CF SMC	136.22 (-8.26%)
AL – ST	138.01 (-7.31%)
AL – TI	135.57 (-9.37%)
AL – ST – TI – CF SMC	130.35 (-12.21%)

When evaluating the mass performance against the baseline, a mass reduction is observed for all four of the MMTO test cases. This is an expected result due to the increase in design freedom allowed by the inclusion of additional materials in the optimization. This clearly demonstrates the benefits of multi-material optimization for conceptual level PAV design. The four-material design exhibits the best results, with a mass reduction of more than 12% when compared to the conventional SMTO approach.

4 Conclusion and Future Work

In this work, MMTO of an eVTOL PAV wing concept under aerodynamic and propulsion loads was conducted. The results of the preliminary MMTO stage indicate a mass reduction of over 12% when compared to conventional SMTO, thus demonstrating the efficacy of MMTO for use in the conceptual design of complex aircraft structures.

The next step for this work will be to develop a higher-fidelity finite element model which directly incorporates VTOL duct, booms, and fuselage joining structures. More in-depth analysis including buckling considerations and more complex loading (roll, yaw, control surface loads) will be investigated. Detailed component-level analysis for manufacturability and identification of candidate components for AM will also be explored.

5 References

[1] J.-H. Zhu, W.-H. Zhang and L. Xia, "Topology Optimization in Aircraft and Aerospace Structures Design," *Archoves of Computational Methods in Engineering*, vol. 23, pp. 595-622, 2016.

[2] M. Tyan, N. V. Nguyen, S. Kim and J.-W. Lee, "Comprehensive preliminary sizing/resizing method for a fixed wing VTOL electric UAV," *Aerospace Science and Technology*, vol. 71, pp. 30-41, 2017.

[3] "Federal Aviation Regulations Part 23 - AIRWORTHINESS STANDARDS: NORMAL CATEGORY AIRPLANES," Federal Aviation Administration, Department of Transportation, Washington, 2021.

[4] N. Glizde, "Plotting the Flight Envelope of an Unmanned Aircraft System Air Vehicle," *Transport and Aerospace Engineering,* vol. 4, pp. 80-87, 2017.

[5] C. F. Hvejsel and E. Lund, "Material interpolation schemes for unified topology and multi-material optimization," *Structural and Multidisciplinary Optimization,* vol. 43, no. 6, pp. 811-825, 2011.